Supplementary Materials: The Hidden Size Effect in Architected Toughness: Critical Length Scales in Layered Materials

Kush Dwivedi[a], Zainab S. Patel[b], Abdulaziz O. Alrashed[a], Ian Good[a], Marco Salviato[c], and Lucas R. Meza[a]

[a] *Mechanical Engineering, University of Washington, Seattle, WA, 98195*
[b] *Materials Science and Engineering, University of Washington, Seattle, WA, 98195*
[c] *William E. Boeing Department of Aeronautics and Astronautics, University of Washington, Seattle, WA, 98195*

Contents

1 Spacer bar sensitivity

Widely spaced architectures (PS, FS) require horizontal spacer bars to prevent layer sagging during development. Because the bars bridge adjacent layers, they carry load and can confound the architectural toughening signal. To isolate their contribution, we fabricated FS specimens ($s/d = 1.6$) with section counts $n = 3$–30 ($n - 1$ spacer bars per beam) and tested them under identical loading conditions.

The initial stiffness and peak load both increase monotonically with n (Fig. S1), confirming that the bars act as parasitic parallel load paths. The curves for $n = 3$–5 cluster together near peak loads of $\sim$3–3.5 mN, while higher counts ($n \geq 10$) produce measurably stiffer responses reaching $\sim$4.5 mN. Specimens with $n = 3$ occasionally exhibited partial layer sagging after development, whereas $n = 5$ (four spacer bars) fully suppressed sagging while remaining in the low-n cluster. We therefore adopted $n = 5$ for all specimens in the main text as the minimum that prevents sagging while minimizing the parasitic mechanical contribution.

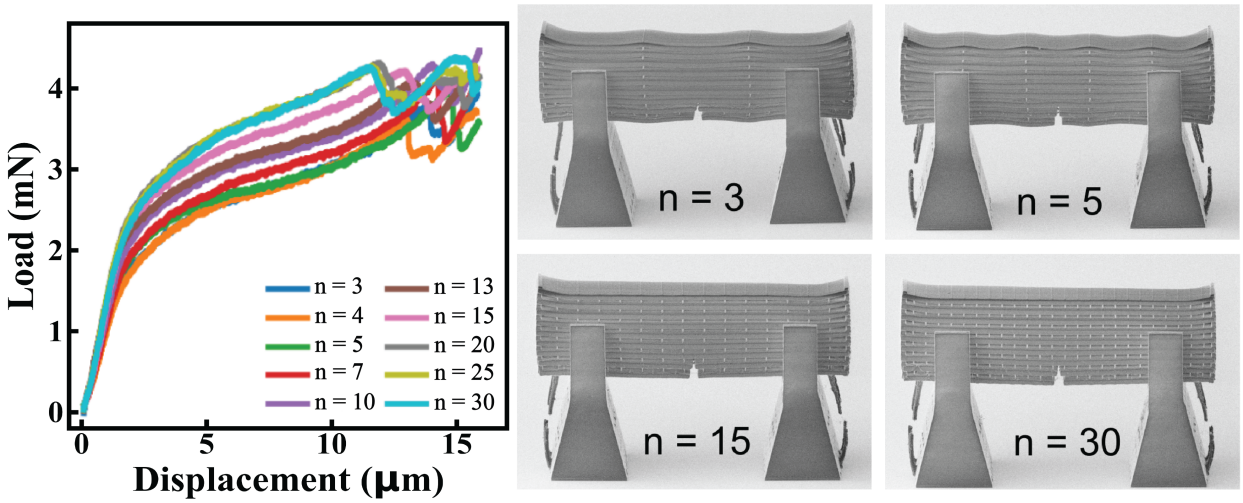

Figure S1: **Spacer-bar sensitivity study.** Left: load–displacement curves for FS-architecture micro-SENB specimens ($s/d = 1.6$) with $n = 3$–30 sections ($n - 1$ spacer bars), tested under identical conditions. Initial stiffness and peak load increase monotonically with n. The low-n curves ($n = 3$–5) cluster together; higher counts ($n \geq 10$) produce a measurably stiffer response. Right: SEM micrographs of representative specimens with $n = 3$, 5, 15, and 30, showing consistent layer geometry across the series. $n = 5$ (four spacer bars) was adopted for all main-text specimens.

2 Friction correction

Polymer-on-polymer contact at the loading supports introduces frictional forces that inflate the measured load–displacement response. To quantify and correct this artifact, we performed matched FEM simulations with penalty friction ($\mu = 0.3$) and without friction ($\mu = 0$) for each architecture.

Figure S2 compares FEM curves with friction (solid lines) against frictionless FEM (dashed lines) for three representative architectures. The simulations with friction reproduce the experimental load–displacement response across the full displacement (main-text Figure 2A), validating the constitutive model and boundary conditions. The frictionless simulations yield lower peak loads by ∼20–35% in the connected architectures (HO, HE, PS), with the offset decreasing in FS where layer decoupling reduces load transfer through the supports.

All quantitative analyses in the main text—including W_f, R_p, and the architectural amplification $\mathcal{A}$—use the frictionless FEM values to isolate the intrinsic mechanical response from the contact artifact. Experimental load–displacement data were corrected by applying the displacement-dependent ratio of frictionless to frictional load extracted from each matched simulation (main-text Methods and Figure **2B**).

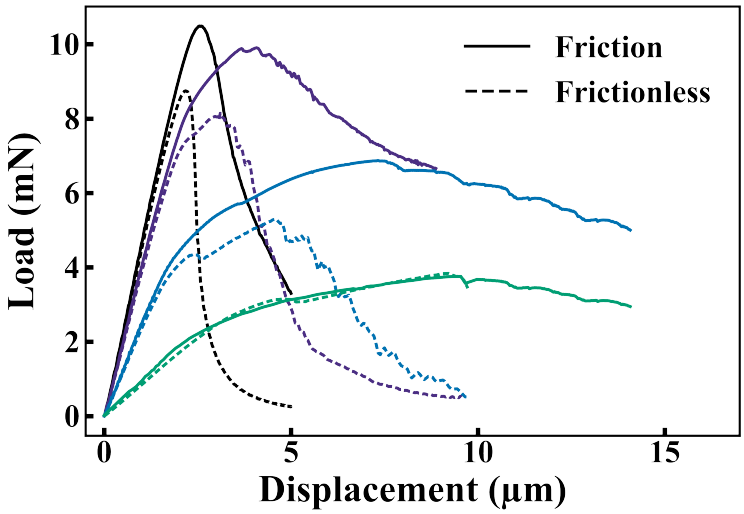

Figure S2: **Friction correction of load–displacement data.** FEM load–displacement curves (solid lines) and frictionless FEM (dashed lines) for three representative architectures. The friction FEM captures the experimental response, confirming that the ∼20–35% peak-load offset between experiment and frictionless FEM (main-text Figure **2B**) is attributable to support friction rather than a constitutive mismatch.

3 Choice of toughness metric: W_f versus J-integral

We adopt the work of fracture W_f (main-text Eq. 1) as the primary toughness metric and report the single-specimen J-integral J_{1L} as a cross-check. W_f is the total energy absorbed during fracture per unit ligament area,

$$W_f = \frac{1}{A_{\text{lig}}} \int_0^{\delta_f} P(\delta)\, \mathrm{d}\delta,$$

computed directly from the global load–displacement response. It makes no assumption about the crack-tip stress state, the local constitutive law, or the crack path, and remains well defined as the architecture departs from homogeneity.

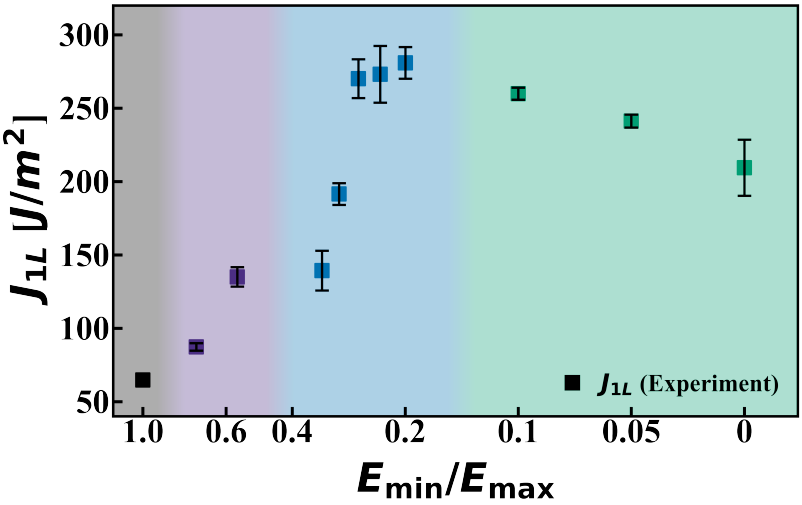

Figure S3: J_{1L} **tracks the architectural trend in** W_f**.** Single-specimen J-integral J_{1L} versus stiffness contrast $E_{\text{min}}/E_{\text{max}}$ for the four architectures, showing a $\sim$4.6$\times$ rise from the homogeneous baseline that mirrors the W_f trend reported in main-text Fig. 3B. Background shading marks the four architectural regimes.

The J-integral, by contrast, is rigorously defined only for a homogeneous, isotropic material under monotonic mode-I loading with a self-similar crack. Both conditions progressively break down in our layered architectures: stiffness varies periodically along the crack front as $E_{\text{min}}/E_{\text{max}}$ decreases, and the crack deflects along compliant interlayers in the more separated architectures, introducing mode-II components that J_{1L} cannot partition. A further practical limitation is that standardized protocols for extracting J_Q or J_{Ic} from microscale J–R data are not yet established, and macroscale ASTM E1820-20b[1] procedures depend sensitively on specimen size and small-scale plasticity. We therefore evaluate J at a crack extension of one layer height, denoted J_{1L}, which provides a consistent comparison basis across architectures even where strict J-validity assumptions are violated.

Despite these limitations, J_{1L} tracks W_f closely across the full architectural sweep (Fig. S3). Both metrics rise monotonically as $E_{\text{min}}/E_{\text{max}}$ decreases, with J_{1L} increasing by $\sim$4.6$\times$ from

the homogeneous baseline and W_f by $\sim 3\times$. The trend agreement confirms that the architectural toughening reported in the main text is robust to the choice of metric.

4 Failure Strain Expression

4.1 Failure strain decomposition

We decompose the failure strain at nominal failure into elastic, plastic, and cohesive softening contributions (figure S4):

$$\varepsilon_f = \underbrace{\frac{\sigma_f}{E}}_{\text{elastic}} + \underbrace{\varepsilon_{p,f}}_{\text{plastic}} + \underbrace{\varepsilon_{\text{soft}}}_{\text{softening}} \tag{1}$$

4.2 Ramberg–Osgood plastic strain and plastic work

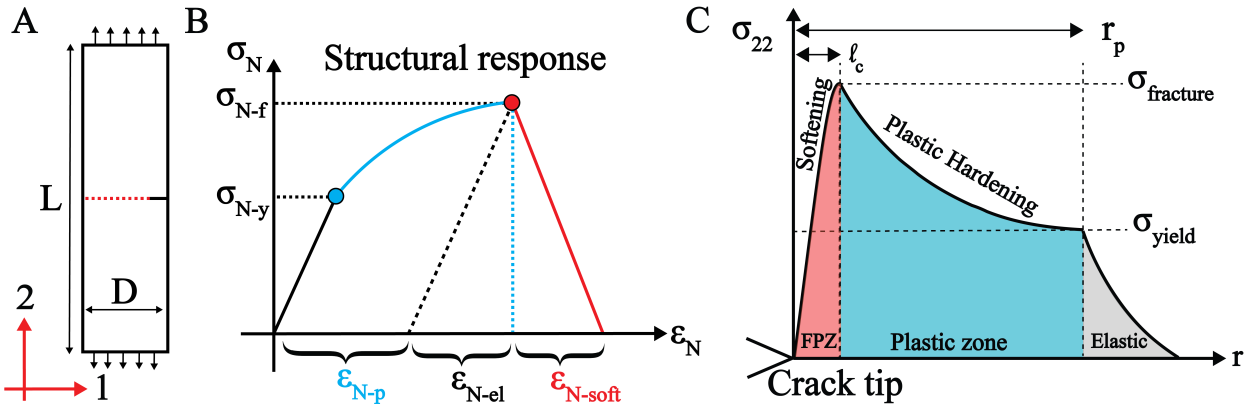

Figure S4: **Schematic illustration of the strain decomposition and length scales used in the failure strain model**. (**A**) Geometry of a SENT specimen of length L and depth D. (**B**) Structural nominal stress–strain response, decomposed into elastic, plastic, and softening contributions. (**C**) Local crack-tip stress distribution $\sigma_{11}(r)$, showing the fracture process zone of size ℓ_c, the plastic zone of size r_p, and the outer elastic region.

We start from a Ramberg–Osgood fit for the total strain

$$\varepsilon(\sigma) = \frac{\sigma}{E} + \alpha \left(\frac{\sigma}{\sigma_y}\right)^n \tag{2}$$

so the plastic part is

$$\varepsilon_p(\sigma) = \alpha \left(\frac{\sigma}{\sigma_y}\right)^n \tag{3}$$

At peak (failure) stress $\sigma = \sigma_f$, the plastic strain is

$$\varepsilon_{p,f} = \alpha \left(\frac{\sigma_f}{\sigma_y}\right)^n \tag{4}$$

We define the plastic work density

$$w_p(\sigma) = \int_0^{\varepsilon_p(\sigma)} \sigma(\varepsilon_p)\, d\varepsilon_p \tag{5}$$

Using the chain rule,

$$d\varepsilon_p = \frac{d\varepsilon_p}{d\sigma}\, d\sigma = \alpha n \frac{\sigma^{n-1}}{\sigma_y^n}\, d\sigma \tag{6}$$

so

$$w_p(\sigma) = \int_0^\sigma \sigma'\, d\varepsilon_p = \int_0^\sigma \sigma' \left(\alpha n \frac{\sigma'^{n-1}}{\sigma_y^n}\right) d\sigma' = \frac{\alpha n}{\sigma_y^n} \int_0^\sigma \sigma'^n\, d\sigma' = \frac{\alpha n}{(n+1)\sigma_y^n} \sigma^{n+1}$$

At start of failure ($\sigma = \sigma_f$) this becomes

$$w_{p,f} = \frac{\alpha n}{n+1} \frac{\sigma_f^{n+1}}{\sigma_y^n} \tag{7}$$

We now assume that this plastic work density is approximately uniform over an effective plastic-zone length r_p, so that the plastic energy per unit crack area is

$$G_p \approx w_{p,f}\, r_p \tag{8}$$

Substituting (7) into (8) gives

$$G_p = \frac{\alpha n}{n+1} \frac{\sigma_f^{n+1}}{\sigma_y^n}\, r_p \tag{9}$$

Rearranging for σ_f,

$$\left(\frac{\sigma_f}{\sigma_y}\right)^{n+1} = \frac{n+1}{\alpha n} \frac{G_p}{r_p \sigma_y} \tag{10}$$

Using (4),

$$\varepsilon_{p,f} = \alpha \left(\frac{\sigma_f}{\sigma_y}\right)^n = \alpha \left[\left(\frac{\sigma_f}{\sigma_y}\right)^{n+1}\right]^{\frac{n}{n+1}} = \alpha \left[\frac{n+1}{\alpha n} \frac{G_p}{r_p \sigma_y}\right]^{\frac{n}{n+1}}$$

We can therefore write the plastic failure strain as

$$\varepsilon_{p,f} = C_p \left(\frac{G_p}{r_p \sigma_y}\right)^{\frac{n}{n+1}} \tag{11}$$

where

$$C_p = \alpha^{\frac{1}{n+1}} \left(\frac{n+1}{n}\right)^{\frac{n}{n+1}} \tag{12}$$

4.3 Relating G_p, G_f, r_p, and ℓ_c

We decompose the total work of fracture into plastic and fracture parts:

$$W_f = G_p + G_f \tag{13}$$

The effective plastic-zone size is taken as

$$r_p = \frac{2}{\pi}\frac{EW_f}{\sigma_y^2} \tag{14}$$

and the fracture process zone length is

$$\ell_c = \frac{EG_f}{\sigma_{f0}^2} \tag{15}$$

From (14)–(15),

$$W_f = \frac{\pi}{2}\frac{\sigma_y^2}{E}\, r_p, \qquad G_f = \frac{\sigma_{f0}^2}{E}\,\ell_c \tag{16}$$

so

$$G_p = W_f - G_f = \frac{\pi}{2}\frac{\sigma_y^2}{E}\, r_p - \frac{\sigma_{f0}^2}{E}\,\ell_c \tag{17}$$

Then

$$\frac{G_p}{r_p\sigma_y} = \frac{\frac{\pi}{2}\frac{\sigma_y^2}{E}\, r_p - \frac{\sigma_{f0}^2}{E}\,\ell_c}{r_p\sigma_y} = \frac{\sigma_y}{E}\left[\frac{\pi}{2} - \left(\frac{\sigma_{f0}}{\sigma_y}\right)^2 \frac{\ell_c}{r_p}\right] \tag{18}$$

Substituting (18) into (11), we obtain

$$\varepsilon_{p,f} = C_p\left[\frac{\sigma_y}{E}\left(\frac{\pi}{2} - \left(\frac{\sigma_{f0}}{\sigma_y}\right)^2 \frac{\ell_c}{r_p}\right)\right]^{\frac{n}{n+1}} \tag{19}$$

4.4 Fracture softening strain

For a linear traction–separation law with cohesive strength σ_{f0} and fracture energy G_f,

$$\delta_c = \frac{2G_f}{\sigma_{f0}} \tag{20}$$

Distributing this opening over a structural length L gives

$$\varepsilon_{\text{soft}} = \frac{\delta_c}{L} = \frac{2G_f}{\sigma_{f0}L} \tag{21}$$

Using $G_f = \sigma_{f0}^2\ell_c/E$ from (15),

$$\varepsilon_{\text{soft}} = \frac{2\sigma_{f0}^2\ell_c}{E\sigma_{f0}L} = \frac{2\sigma_{f0}\ell_c}{EL} \tag{22}$$

For single edge notch fracture we take $L = 4D$, so

$$\varepsilon_{\text{soft}} = \frac{2\sigma_{f0}\ell_c}{E(4D)} = \frac{\sigma_{f0}\ell_c}{2ED} \tag{23}$$

4.5 Bažant size-effect law

The nominal stress at failure follows a Bažant-type SEL:

$$\sigma_f = \frac{\sigma_{f0}}{\sqrt{1 + D/D_0}} \tag{24}$$

so the elastic strain is

$$\frac{\sigma_f}{E} = \frac{\sigma_{f0}}{E\sqrt{1 + D/D_0}} \tag{25}$$

4.6 Failure strain expression

Substituting the elastic term (25), the plastic term (19), and the softening term (23) into the decomposition (1) gives

$$\varepsilon_f(D) = \frac{\sigma_{f0}}{E\sqrt{1 + D/D_0}} + C_p \left[\frac{\sigma_y}{E} \left(\frac{\pi}{2} - \left(\frac{\sigma_{f0}}{\sigma_y} \right)^2 \frac{\ell_c}{r_p} \right) \right]^{\frac{n}{n+1}} + \frac{\sigma_{f0}\ell_c}{2ED} \tag{26}$$

Equivalently, using $G_p = W_f - G_f$ together with Eqs. (14) and (15), Eq. (26) can be recast in terms of energy quantities:

$$\varepsilon_f(D) = \frac{\sigma_{f0}}{E\sqrt{1 + D/D_0}} + C_p \left[\frac{\pi}{2} \left(\frac{\sigma_y}{E} \right) \left(\frac{G_p}{W_f} \right) \right]^{\frac{n}{n+1}} + \frac{G_f}{2\sigma_{f0}D} \tag{27}$$

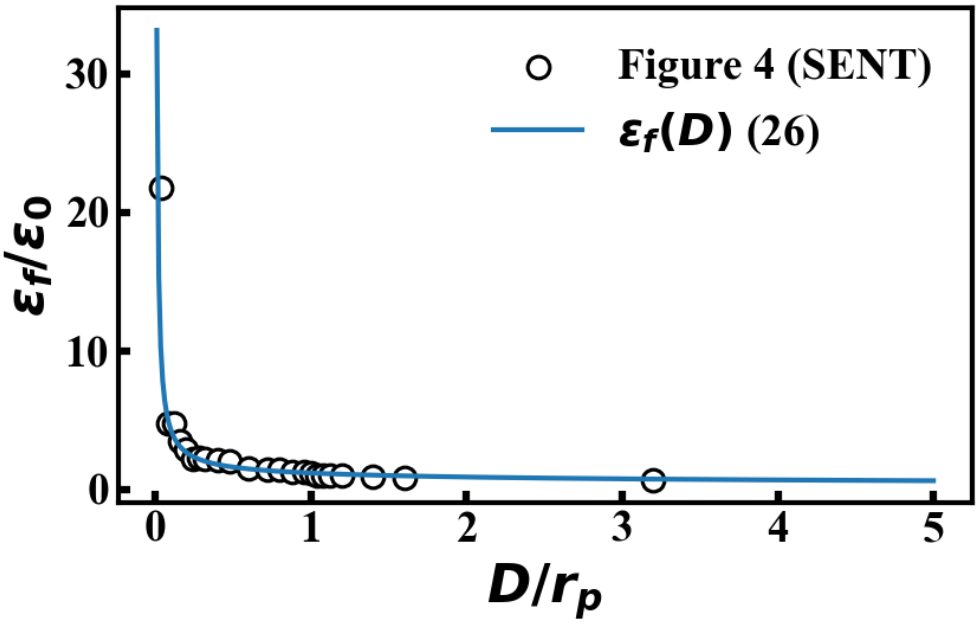

Figure S5: **Closed-form failure strain $\varepsilon_f(D)$ validated against SENT simulation data.** The model of Eq. (26) (solid line) is plotted against the simulated failure strains from main-text Figure 4 across the architectural sweep. Material constants (σ_{f0}, σ_y, E, D_0, n, α) are calibrated to the homogeneous baseline; the D-dependence and the architectural variation in r_p and ℓ_c are predicted, not fit.

5 Architectural Amplification

This section derives the architectural amplification factor $\mathcal{A}$ for a layered composite of alternating hard (H) and soft (S) phases with a crack propagating perpendicular to the interfaces. Figure S6 provides a visual overview: the crack path deflects and arrests at material interfaces, and the cyan field marks the local plastic zone at the crack tip, which extends laterally into the softer phases and into the hard phase beyond the monolithic baseline $r_p^{(H)}$. Panel B places this local picture in the SENT specimen, where the plastic strain ε_p is concentrated along the ligament and $D \gg r_p$, ensuring contained yielding. Together, these motivate the four additive contributions to $\mathcal{A}$ derived below: a rule-of-mixtures baseline, crack reinitiation at stiffness-contrast interfaces, crack path tortuosity, and enhanced hard-phase plasticity from cross-phase process zone interaction.

5.1 Governing assumptions

We consider a layered composite with two dimensionless material contrasts that appear throughout:

$$\eta \equiv \frac{E_H}{E_S}, \qquad \phi \equiv \frac{G_f^S}{G_f^H}, \tag{28}$$

together with the soft-phase volume fraction f_v, the strength ratio σ_y^H/σ_y^S, and the power-law hardening exponent n. A central distinction in this framework is the separation of the

fracture energy G_f from the total work of fracture $W_f = G_f + G_p$, where G_p is the plastic dissipation. Different toughening mechanisms draw on different parts of this energy budget:

- **Crack surface creation** (reinitiation, tortuosity): governed by G_f, because crack arrest and deflection depend on whether the elastic stress intensity can supply the energy to create new fracture surfaces.
- **Bulk dissipation** (rule of mixtures, process zone interaction): governed by W_f, because the total energy absorbed per unit crack area includes both surface creation and plastic work in the surrounding process zone.

The process zone radius reflects the total energy balance and is defined in terms of W_f, using the Irwin form with the standard factor-of-two correction for stress redistribution from yielding:

$$r_p = \frac{2}{\pi}\frac{E\,W_f}{\sigma_y^2} \tag{29}$$

The effective work of fracture of the composite, normalized by W_f^H, has four additive contributions:

$$\boxed{\frac{W_f^{\text{eff}}}{W_f^H} = \underbrace{\text{ROM}}_{\text{Rule of mixtures}} + \underbrace{\Delta W_{\text{ini}}}_{\substack{\text{Crack}\\ \text{reinitiation}}} + \underbrace{\Delta W_{\text{tort}}}_{\substack{\text{Crack path}\\ \text{deflection}}} + \underbrace{\Delta W_{\text{int}}}_{\substack{\text{Process zone}\\ \text{interaction}}}} \tag{30}$$

The first term captures each phase's intrinsic toughness, including its own plasticity. The second and third terms are interface-level mechanisms that depend on fracture surfaces. The fourth term captures the synergistic cross-phase dissipation that arises only because the phases are adjacent.

5.2 Component 1: Rule-of-mixtures baseline (uses W_f)

For a straight-through crack traversing alternating layers, each layer dissipates its own full work of fracture, and the volume-weighted average gives

$$\boxed{\frac{\text{ROM}}{W_f^H} = (1 - f_v) + f_v\,\frac{W_f^S}{W_f^H}} \tag{31}$$

This term captures each phase's intrinsic toughness contribution, including its own plastic dissipation, but it does not include any architectural coupling between phases.

5.3 Component 2: Crack reinitiation (uses G_f)

Crack propagation under small-scale yielding requires the elastic energy release rate to exceed the fracture energy, $(K_I^{\text{applied}})^2/E \geq G_f$. The relevant threshold is G_f, not W_f: arrest is governed by whether the elastic K-field can supply energy for new fracture surfaces, and the plastic zone only develops locally after the crack enters the new layer.

H→S transition. When the crack exits H at steady state, $(K_I^{\text{applied}})^2 = E_H\, G_f^H$. Entering S, $G\big|_{\text{in S}} = \eta\, G_f^H$, so propagation requires $\eta \geq \phi$. The crack therefore arrests at H→S when $\phi > \eta$, with an energy deficit per crossing of $\Delta G = (\phi - \eta)\, G_f^H$.

S→H transition. By the same argument, $G\big|_{\text{in H}} = G_f^S/\eta$, and the crack passes through whenever $G_f^S/\eta \geq G_f^H$, i.e. $\eta \leq \phi$. The two transitions are mutually exclusive: a single inequality between η and ϕ determines which interface is energetically deficient.

Reinitiation cost. Each period contains one arresting interface. Normalizing by W_f^H:

$$\boxed{\frac{\Delta W_{\text{ini}}}{W_f^H} = \begin{cases} (\phi - \eta)\,\dfrac{G_f^H}{W_f^H}, & \eta < \phi \quad \text{(H→S arrests)} \\ \left(1 - \dfrac{\phi}{\eta}\right)\dfrac{G_f^H}{W_f^H}, & \eta > \phi \quad \text{(S→H arrests)} \\ 0, & \eta = \phi \end{cases}} \tag{32}$$

For the HE reference architecture ($\eta = 1.79$, $\phi = 2.13$), H→S is the arresting interface.

5.4 Component 3: Crack path tortuosity (uses G_f)

If the crack deflects by a distance δ along each interface before re-entering the next layer, the additional fracture surfaces created lengthen the crack path. Assuming the interface fracture energy is comparable to G_f^S:

$$\boxed{\frac{\Delta W_{\text{tort}}}{W_f^H} = \phi\,\frac{G_f^H}{W_f^H}\,\frac{2\delta}{\lambda}} \tag{33}$$

where λ is the layer period. When no crack deflection is observed ($\delta = 0$), this term vanishes; this is the case for all architectures considered here.

5.5 Component 4: Enhanced hard-phase plasticity (uses W_f)

In a monolithic hard specimen, the plastic zone at the crack tip is laterally constrained by the surrounding hard material, producing the standard plane-strain zone of size $r_p^{(H)}$. In the layered composite, adjacent compliant phases release this lateral constraint and the hard-phase plastic zone extends to an effective radius $\tilde{r}_p^{(H)} = \kappa\, r_p^{(H)}$, with $\kappa \geq 1$ a dimensionless constraint-release factor. The extra dissipation in this annulus is the architectural toughening that the ROM cannot capture, since the ROM treats each phase as fracturing in isolation with its own process zone.

5.5.1 Two regimes of constraint release

Constraint release can occur through two physically distinct mechanisms, and κ takes very different values in each.

Passive (geometric) regime: $1 \leq \kappa \leq 3$**.** When the neighbor does not transmit load to the hard phase — a free surface, a vacuum gap, or a rigid wall with no displacement coupling — the constraint release is purely geometric. The classical plane-stress/plane-strain transition lies in this regime:[2] a free lateral surface relaxes triaxial constraint and inflates the plastic-zone radius by at most a factor of three, so $\kappa \leq 3$ at full plane-stress. Bonded but stiffer neighbors fall on the opposite end ($\kappa < 1$, anti-shielding), recovering the crack-tip shielding effect documented at strength-mismatched bimaterial interfaces.[3–6] The whole passive regime is bracketed by $\kappa \in [0, 3]$, and three is a hard upper bound.

Active (compatibility-driven) regime: κ **can far exceed three.** When the neighbor is bonded and plastically yielding, a qualitatively different mechanism operates. At the H–S interface, displacement compatibility ties the hard-phase strain to the soft-phase strain. In the annulus $r_p^{(H)} < r < r_p^{(S)}$, the soft phase is plastic and develops HRR-type strains far exceeding the hard phase's local elastic strain. The soft phase therefore drags the hard phase through the bonded interface, forcing it into plastic deformation at radii where, on its own, the hard phase would remain elastic. This is not passive constraint release but active compatibility-driven plasticization, and there is no upper-bound argument analogous to the geometric factor of three. The effective κ in this regime is set by the H–S contrast and can be much larger.
The bioinspired material inhomogeneity effect[7] also belongs to this active regime, although it is usually presented without separating it from the passive geometric factor. We treat the two regimes explicitly because they have different limits and different governing physics. The architectures studied here (HE, PS, FS) all sit in the active regime; architectures with vanishing interlayer modulus sit between the two regimes, where neither mechanism operates effectively, since the gap loses load transfer before the passive limit is approached.

5.5.2 Physical picture

Figure S6A superposes the plastic-zone contours of a monolithic hard specimen and the layered composite at the same far-field load. Two features stand out. First, each soft layer develops horizontal plastic bands extending well beyond the hard layers; these are the soft phase's own process zone, an intrinsic property already accounted for by $f_v\, W_f^S$ in the ROM. Second, the hard-layer plastic zone in the composite extends past the monolithic baseline $r_p^{(H)}$. At distances $r_p^{(H)} < r < r_p^{(S)}$, the local opening stress is below σ_y^H but above σ_y^S: the soft phase yields, displacement compatibility at the bonded interface transmits the soft-phase plastic strain into the hard phase, and the hard phase is forced into yield at radii where, on its own, it would remain elastic. The dissipation rate of the hard phase in this annulus therefore tracks the soft-phase HRR work density, because compatibility, not the hard phase's own stress field, sets the local plastic strain.

5.5.3 Derivation of the interaction term

Cross-phase plastic annulus. Under the hard-phase K_I-field, the local opening stress is $\sigma(r) = K_I/\sqrt{2\pi r}$. The soft-phase yield condition $\sigma(r) = \sigma_y^S$ defines a soft-phase plastic

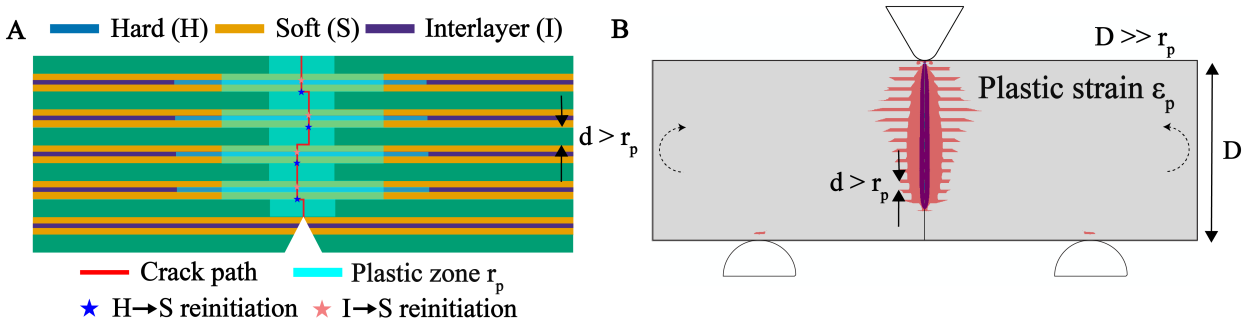

Figure S6: **Architectural toughening mechanisms and process zone interaction.** **A**, Simulated plastic zone in a three-phase layered architecture. The crack path (red) arrests and reinitiates at H→S (blue stars) and I→S (pink stars) interfaces. The plastic zone r_p (cyan) extends laterally into the soft and interlayer phases, and enhances hard-phase plasticity beyond the monolithic baseline. The layer height satisfies $d > r_p$, the separation-of-zones condition required for the derivation in §5.5.3 (distinct from the layer-scale optimality condition $d \approx r_p$ in the main text). **B**, SENT specimen schematic showing the plastic strain field ε_p concentrated along the ligament, with $D \gg r_p$ ensuring contained yielding within the size-effect regime.

radius

$$r_p^{(S)} = \left(\frac{\sigma_y^H}{\sigma_y^S}\right)^2 r_p^{(H)} \tag{34}$$

which exceeds $r_p^{(H)}$ whenever $\sigma_y^H > \sigma_y^S$. The annulus $r_p^{(H)} < r < r_p^{(S)}$ is the geometric extent over which the soft phase yields plastically under the hard-phase K_I-field but the hard phase, on its own, would be elastic. This annulus is what the architecture activates.

Soft-phase HRR work density. Within the soft-phase plastic zone, the HRR singular field gives $\sigma(r) \propto r^{-1/(n+1)}$ and $\varepsilon_p(r) \propto r^{-n/(n+1)}$, so the soft-phase plastic work density falls as $1/r$:[2,7]

$$w_p^{(S)}(r) = \frac{n}{n+1}\frac{(\sigma_y^S)^2}{E_S}\frac{r_p^{(S)}}{r} \tag{35}$$

Displacement compatibility at the bonded H–S interface enforces $\varepsilon_p^{(H)}(r) = \varepsilon_p^{(S)}(r)$. The hard phase is at yield (stress σ_y^H) while accommodating the soft-phase strain, so it dissipates at a rate that tracks $w_p^{(S)}(r)$ rather than its own much smaller monolithic value.

Integration over the annulus. Integrating $w_p^{(S)}(r)$ over the annulus $[r_p^{(H)}, r_p^{(S)}]$, doubled to account for both sides of the planar crack and weighted by the fraction f_v of crack-front length adjacent to an H–S interface,

$$\begin{aligned}\Delta W_{\text{int}} &= 2\,f_v \int_{r_p^{(H)}}^{r_p^{(S)}} w_p^{(S)}(r)\,dr = 2\,f_v\,\frac{n}{n+1}\frac{(\sigma_y^S)^2}{E_S}\,r_p^{(S)}\,\ln\left(\frac{r_p^{(S)}}{r_p^{(H)}}\right)\\ &= 4\,f_v\,\frac{n}{n+1}\frac{(\sigma_y^S)^2}{E_S}\,r_p^{(S)}\,\ln\left(\frac{\sigma_y^H}{\sigma_y^S}\right)\end{aligned} \tag{36}$$

where the second line uses Eq. (34). The geometric prefactor $(\sigma_y^S)^2 r_p^{(S)}/E_S$ simplifies using Eq. (34) and the Irwin balance $(\sigma_y^H)^2 r_p^{(H)}/E_H = (2/\pi)\, W_f^H$:

$$\frac{(\sigma_y^S)^2 r_p^{(S)}}{E_S} = \frac{(\sigma_y^S)^2}{E_S}\left(\frac{\sigma_y^H}{\sigma_y^S}\right)^2 r_p^{(H)} = \frac{(\sigma_y^H)^2 r_p^{(H)}}{E_H}\cdot\frac{E_H}{E_S} = \frac{2}{\pi}\,\eta\, W_f^H \tag{37}$$

Substituting back and normalizing by W_f^H,

$$\boxed{\frac{\Delta W_{\text{int}}}{W_f^H} = \frac{8\, f_v\, \eta\, n}{(n+1)\,\pi}\,\ln\!\left(\frac{\sigma_y^H}{\sigma_y^S}\right)} \tag{38}$$

This is the expression used in the main text. It depends only on the two dimensionless material contrasts (η and σ_y^H/σ_y^S), the soft-phase volume fraction f_v, and the hardening exponent n; the absolute magnitudes of r_p, layer thickness, and W_f^H all cancel.

Effective active κ. Comparing Eq. (38) to the canonical form $\Delta W_{\text{int}}/W_f^H = (4 f_v n/[(n+1)\pi])\ln\kappa$ that would arise from a hard-phase HRR integral over $[r_p^{(H)}, \kappa\, r_p^{(H)}]$ yields the effective active-regime value

$$\ln\kappa_{\text{eff}} = 2\,\eta\,\ln\!\left(\frac{\sigma_y^H}{\sigma_y^S}\right) \tag{39}$$

For the HE reference architecture ($\eta = 1.79$, $\sigma_y^H/\sigma_y^S \approx 2.2$), $\kappa_{\text{eff}} \approx 17$, far above the passive upper bound of three. This is the quantitative signature of the active regime: the soft phase pumps energy into the hard phase through compatibility, an effect that has no analogue in the geometric plane-stress/plane-strain limit.

5.5.4 Domain of validity

The derivation requires three conditions: (i) the H–S interface is bonded, so traction and displacement are both continuous; (ii) the soft phase yields plastically at the relevant length scale and is a load-bearing solid with finite σ_y^S, not vacuum; and (iii) the hard and soft phases share the same hardening exponent n, consistent with the present polymer-on-polymer system. Three boundary cases are worth flagging:

- **Free surface or air gap.** As the soft phase approaches a non-load-transmitting limit, condition (i) fails: there is no compatibility to enforce, and the active mechanism shuts off. The system crosses into the passive regime ($\kappa \leq 3$), but other architectural losses — loss of load transfer between hard layers, crack deflection along the gap — dominate before the passive plane-stress limit is reached. Architectures with vanishing interlayer modulus sit in this transitional region, and Eq. (38) is not used there; the observed de-toughening at very high s/d is attributable to load-transfer loss rather than to a vanishing interaction term.

- **Stiffer neighbor.** If the neighbor has higher modulus or yield strength, compatibility suppresses rather than enhances hard-phase plastic strain, and the effect becomes anti-shielding. This recovers the bimaterial shielding mechanism of refs.[3,5] as the inverse case.

- **Soft-phase enhancement.** The soft phase already yields under its own monolithic K-field at any r in the annulus, so its plastic strains are largely insensitive to the boundary condition imposed by the hard phase. The hard phase, by contrast, transitions from elastic (monolith) to plastic (composite), so the change in its dissipation is first-order; any residual soft-phase enhancement enters at higher order and is absorbed into the calibrated W_f^S in the ROM.

5.6 Total architectural amplification (two-phase)

Combining all four components,

$$\mathcal{A} = (1 - f_v) + f_v \frac{W_f^S}{W_f^H} + (\phi - \eta) \frac{G_f^H}{W_f^H} + \phi \frac{G_f^H}{W_f^H} \frac{2\delta}{\lambda} + \frac{8\, f_v\, \eta\, n}{(n+1)\,\pi} \ln\left(\frac{\sigma_y^H}{\sigma_y^S}\right) \tag{40}$$

which is Eq. (6) of the main text.

5.7 Extension to three-material architectures

We extend the framework to three-material layered systems with stacking sequence

$$\underbrace{H(t_H)}_{\text{hard}} - \underbrace{S(t_S)}_{\text{soft}} - \underbrace{I(t_I)}_{\text{interlayer}} - \underbrace{S(t_S)}_{\text{soft}} - [\text{repeat}], \tag{41}$$

so the period is $\lambda = t_H + 2t_S + t_I$, with $t_H = 1.0$ μm and $t_S = 0.3$ μm. The interlayer thickness t_I varies with the architectural spacing S as $t_I = S - 1.6$ μm.

ROM (three-phase). Each phase contributes its own W_f weighted by volume fraction:

$$\frac{\text{ROM}}{W_f^H} = f_H + f_S \frac{W_f^S}{W_f^H} + f_I \frac{W_f^I}{W_f^H} \tag{42}$$

Reinitiation (three-phase). Each period contains four interfaces: H/S, S/I, I/S, S/H. Applying the analysis of §5.3 to each shows that only H→S and I→S arrest under the present property contrasts; S→H and S→I have surplus G and pass through. The I→S deficit is

$$\frac{\Delta W_{\text{I}\to\text{S}}}{W_f^H} = \frac{G_f^H}{W_f^H} \max\left(\frac{G_f^S}{G_f^H} - \frac{E_I}{E_S}\frac{G_f^I}{G_f^H},\, 0\right) \tag{43}$$

and is added to the H→S contribution from Eq. (32).

Interaction (three-phase). In the H–S–I–S stacking, the hard phase is bonded only to soft layers and no H–I interface exists. The interlayer therefore does not directly modify the hard phase's constraint state, and the interaction term retains its two-phase form with the H–S contrast parameters but uses the three-phase f_S (which differs from the two-phase value because the interlayer occupies part of the period):

$$\frac{\Delta W_{\text{int}}}{W_f^H} = \frac{8\, f_S\, \eta\, n}{(n+1)\,\pi}\, \ln\left(\frac{\sigma_y^H}{\sigma_y^S}\right) \tag{44}$$

The interlayer contributes to toughness through its intrinsic W_f^I (in the ROM) and through the I→S arrest event (in reinitiation), but not through the interaction term.

5.8 Application to layered architectures

We evaluate Eq. (40) (two-phase) and Eqs. (42)–(44) (three-phase) across the eleven architectures shown in main-text Figure 5A. Hard-phase properties are fixed at $E_H = 2.5$ GPa, $\sigma_y^H = 50$ MPa, $G_f^H = 20$ J/m^2, $W_f^H = 69$ J/m^2; soft and interlayer properties vary with layer spacing and are listed in Table 1. The hard-phase layer height is $d = 1.6$ μm (the full TPL voxel height); the dimensionless architectural ratio is $s/d = S/d$.

Table 1: **Spacing-resolved phase properties and volume fractions used to evaluate $\mathcal{A}$ in main-text Figure 5.** The HO architecture ($s/d = 0.63$) contains only the hard phase. Two-phase architectures (HE) have $f_I = 0$ and no interlayer (em-dashes).

		Hard phase (H)				Soft phase (S)				Interlayer (I)				Volume fraction		
s/d	$E_{\min}/E_{\max}$	E_H GPa	σ_y^H MPa	G_f^H J/m^2	W_f^H J/m^2	E_S GPa	σ_y^S MPa	G_f^S J/m^2	W_f^S J/m^2	E_I GPa	σ_y^I MPa	G_f^I J/m^2	W_f^I J/m^2	f_H	f_S	f_I
0.63	1.00	2.50	50.0	20.0	69	—	—	—	—	—	—	—	—	1.000	0.000	0.000
0.81	0.72	2.50	50.0	20.0	69	1.80	28.0	33.0	110	—	—	—	—	0.625	0.375	0.000
0.94	0.56	2.50	50.0	20.0	69	1.40	22.5	42.5	150	—	—	—	—	0.625	0.375	0.000
1.00	0.50	2.50	50.0	20.0	69	1.25	20.1	40.0	130	—	—	—	—	0.625	0.375	0.000
1.06	0.33	2.50	50.0	20.0	69	1.25	20.1	40.0	130	0.833	14.0	26.6	103	0.588	0.353	0.059
1.19	0.30	2.50	50.0	20.0	69	1.25	20.1	40.0	130	0.750	13.0	25.0	90	0.526	0.316	0.158
1.31	0.27	2.50	50.0	20.0	69	1.25	20.1	40.0	130	0.667	12.0	23.3	76.7	0.476	0.286	0.238
1.44	0.23	2.50	50.0	20.0	69	1.25	20.1	40.0	130	0.583	11.0	21.7	63.7	0.435	0.261	0.304
1.56	0.20	2.50	50.0	20.0	69	1.25	20.1	40.0	130	0.500	10.0	20.0	50	0.400	0.240	0.360
1.69	0.10	2.50	50.0	20.0	69	1.25	20.1	40.0	130	0.250	7.5	15.0	40	0.370	0.222	0.407
1.81	0.05	2.50	50.0	20.0	69	1.25	20.1	40.0	130	0.125	2.5	5.0	10	0.345	0.207	0.448

Table 2 reports the component-wise decomposition of $\mathcal{A}$ at three representative architectures spanning the HE–PS–FS sweep, computed with the spacing-resolved properties of Table 1. The model agrees with the simulated $\mathcal{A}_{\text{sim}}$ to within $\sim 7\%$ with no adjustable parameters; values across the full architectural sweep are plotted in main-text Figure 5A.

The decomposition explains the non-monotonic $\mathcal{A}(s/d)$ in main-text Figure 5A. From HE through PS, the ROM saturates near 1.4 while reinitiation activates and interaction climbs as the H–S contrast grows, driving $\mathcal{A}$ to its peak of 3.15 at $s/d \approx 1.06$. From PS through FS, the soft-phase volume fraction $f_S = 2t_S/\lambda$ falls as λ grows, eroding both the ROM and the interaction term faster than reinitiation can compensate; $\mathcal{A}$ declines. Beyond $s/d \approx 1.8$, the interlayer modulus approaches zero and the system crosses into the load-transfer-loss regime (§5.5.4), where the framework no longer applies.

Table 2: **Component-wise decomposition of $\mathcal{A}$ at representative HE, PS, and FS architectures.** Tortuosity vanishes ($\delta = 0$) in all cases and is omitted. $\mathcal{A}_{\text{sim}}$ is from frictionless FEM at $d \gg r_p$.

	s/d	ROM	Reinit.	Interaction	$\boldsymbol{\mathcal{A}}$	$\mathcal{A}_{\text{sim}}$	Error
HE	0.94	1.44	0.10	1.24	**2.78**	2.60	+6.9%
PS	1.06	1.34	0.32	1.49	**3.15**	3.10	+1.6%
FS	1.56	1.11	0.46	1.01	**2.59**	2.77	−6.5%

6 Length-scale calculations for natural laminates

We apply main-text Eq. 2, $R_p \approx E\,W_f/\sigma_f^2$, to nacre and *Euplectella* spicules at the composite scale. Reported properties below are those of the layered composite (not the brittle constituent). The structural-scale condition $D \approx 2R_p$ reflects the bending configuration (main-text Figure 6A); the layer-scale dimensional match $d \approx \ell_c$ is discussed in the main text.

6.1 Nacre

For dry nacre:[8] $E = 70$ GPa, $\sigma_f = 170$ MPa, and $W_f = 350$–1000 J/m^2 (Jackson *et al.* report 350–1240 J/m^2 across hydration states; we adopt 350–1000 J/m^2). This gives $R_p \approx 0.85$–2.42 mm, matching the observed nacre layer thickness of ∼0.5–2 mm.[9,10] Nacre therefore satisfies $D \approx 2R_p$ at a single hierarchical level.

6.2 *Euplectella* spicule

For the spicule:[11–14] $E \approx 28$–46 GPa, $\sigma_f \approx 74$–125 MPa, and $W_f \lesssim 50$ J/m^2, consistent with the modest architectural amplification reported by Monn & Kesari.[14] This gives $R_p \approx 0.07$–0.42 mm, so $2R_p \approx 0.14$–0.84 mm, well above the spicule diameter of ∼50 μm. The spicule therefore lies in the truncated regime ($D < 2R_p$), with curved lamellar geometry further limiting $\mathcal{A}$ and keeping R_p from growing larger.

References

[1] ASTM E1820-18. Standard test method for measurement of fracture toughness. Technical report, ASTM, 2011.

[2] T. L. Anderson. *Fracture Mechanics: Fundamentals and Applications*. CRC Press, Boca Raton, 3 edition, 2005.

[3] Y. Sugimura, P. G. Lim, C. F. Shih, and S. Suresh. Fracture normal to a bimaterial interface: Effects of plasticity on crack-tip shielding and amplification. *Acta Metallurgica et Materialia*, 43(3):1157–1169, 1995.

[4] S. Suresh, Y. Sugimura, and E. K. Tschegg. The growth of a fatigue crack approaching a perpendicularly-oriented bimaterial interface. *Scripta Metallurgica et Materialia*, 27(9):1189–1194, 1992.

[5] A. S. Kim, S. Suresh, and C. F. Shih. Plasticity effects on fracture normal to interfaces with homogeneous and graded compositions. *International Journal of Solids and Structures*, 34(26):3415–3432, 1997.

[6] R. Pippan, K. Flechsig, and F. O. Riemelmoser. Fatigue crack propagation behavior in the vicinity of an interface between materials with different yield stresses. *Materials Science and Engineering A*, 283(1–2):225–233, 2000.

[7] V. Tvergaard and J. W. Hutchinson. The relation between crack growth resistance and fracture process parameters in elastic–plastic solids. *Journal of the Mechanics and Physics of Solids*, 40(6):1377–1397, 1992.

[8] A. P. Jackson, J. F. V. Vincent, and R. M. Turner. The mechanical design of nacre. *Proceedings of the Royal Society B: Biological Sciences*, 234(1277):415–440, 1988.

[9] Horacio D. Espinosa, Allison L. Juster, Felix J. Latourte, Owen Y. Loh, David Gregoire, and Pablo D. Zavattieri. Tablet-level origin of toughening in abalone shells and translation to synthetic composite materials. *Nature Communications*, 2(1):173, 2011.

[10] A. Zhang, H. Price, Y. Chen, and B. C. Prorok. Reversible tablet sliding and strain-limited deformation in nacre: In-situ observations and threshold determination. *Experimental Mechanics*, 66(1):163–173, 2026.

[11] Joanna Aizenberg, James C Weaver, Monica S Thanawala, Vikram C Sundar, Daniel E Morse, and Peter Fratzl. Skeleton of euplectella sp.: structural hierarchy from the nanoscale to the macroscale. *Science*, 309(5732):275–278, 2005.

[12] Milene C. Fernandes, Joanna Aizenberg, James C. Weaver, and Katia Bertoldi. Mechanically robust lattices inspired by deep-sea glass sponges. *Nature Materials*, 20:237–241, 2021.

[13] Michael A. Monn, James C. Weaver, Tianyang Zhang, Joanna Aizenberg, and Haneesh Kesari. New functional insights into the internal architecture of the laminated anchor spicules of *euplectella aspergillum*. *Proceedings of the National Academy of Sciences*, 112(16):4976–4981, 2015.

[14] Michael A. Monn, Kaushik Vijaykumar, Sayaka Kochiyama, and Haneesh Kesari. Lamellar architectures in stiff biomaterials may not always be templates for enhancing toughness in composites. *Nature Communications*, 11(1):373, January 2020.